Ceramics-Silikáty 68 (1), 132-142 (2024)
www.ceramics-silikaty.cz doi: 10.13168/cs.2024.0012

SYNTHESIS OF NaY ZEOLITE FROM WATER QUENCHING SLAG AND ITS APPLICATION IN CO_2 CAPTURE

SHUAI CHE*, #SHIHAI SUN*, XIAOCHENG YU*, RUI HUANG*, XIANHE CHEN*, YINGAI ZHU**

** School of Mechanical and Power Engineering, Shenyang University of Chemical Technology, Shenyang 110142, China*
***Shenyang Emergency Center, Shenyang, China*

#E-mail: sshjv0322@163.com

Submitted January 4, 2024, accepted February 19, 2024

Keywords: Water quenching slag, Synthesis, NaY zeolite, CO_2 capture, Flue gases, Adsorption capacity

In order to reduce costs and environmental hazards, this article explores a new synthesis method for preparing NaY zeolite using water quenching residue as the raw material. The effects of the crystallisation time, crystallisation temperature, $n(SiO_2)/n(Al_2O_3)$ ratio and $n(Na_2O)/n(Al_2O_3)$ ratio on the crystallisation of NaY zeolite were investigated, and an ideal synthetic route was obtained. The physical and chemical properties of the prepared NaY zeolite were characterised by XRD, SEM, STEM, FTIR and other methods. In order to understand the adsorption performance of the prepared Y zeolite, different adsorption isotherm models were studied at 30 °C, 60 °C, 90 °C and 0 to 1 bar. At these three temperatures, NaY zeolite has a much higher adsorption capacity for CO_2 than N_2. The Toth equation fits well the CO_2 adsorption of NaY zeolite. The BET test calculates that the micropore specific surface area of NaY zeolite is 838.88 $m^2 \cdot g^{-1}$. The range of the zeolite micropores is mainly between 0.35 ~ 0.45 nm. The NaY zeolite obtained by the technical route reported in this study has high crystallinity, a uniform particle size, high thermal stability, and excellent CO_2 adsorption performance under flue gas conditions, and will have potential applications in the CO_2 capture in steel plant flue gas prospect.

INTRODUCTION

As a kind of blast furnace slag, water quenching slag is mainly composed of calcium, magnesium, manganese and other oxides and aluminosilicates. According to statistics, about 220 million tonnes of water quenching slag are produced in China every year [1, 2]. The huge stock of water quenching slag has an irreversible impact on and causes harm to the groundwater, climate and soil [3]. Therefore, it is very important to utilise water quenching slag as a resource and increase its added value. At present, the main utilisation of water quenching slag is to repair inorganic fertilisers, ceramic materials, glass and cement of which 90 % are used as cement materials [5-8]. However, due to the impact of the economic downturn and environmental factors, the cement industry was forced to reduce the production scale and the use of water quenching slag as a cementitious material also decreased accordingly [9]. At present, the utilisation of water quenching slag has reached a saturation point, and it is very necessary and urgent to seek new treatment methods to promote the sustainable development of the steel industry.

The main components of water quenching slag are CaO, SiO_2 and Al_2O_3, with a small amount of metal oxides such as MgO and Fe_2O_3, and the Al_2O_3 and SiO_2 contained in it are the elemental materials of synthetic zeolite [10]. NaY zeolite is a crystalline material with a Faujasite (FAU) framework structure [22]. The main structure is a truncated octahedral framework composed of silicon-oxygen tetrahedrons and oxygen-aluminium tetrahedrons linked by oxygen atoms [11]. Each octahedron is connected with the other four basic units through a hexagonal prism according to the tetrahedral structure to form a Y zeolite crystal. Due to its unique structure and surface properties, Y zeolite is widely used in the catalysis, adsorption and separation fields [12-14]. Compared with ZSM-5, *β*-zeolite, and A-type zeolite, Y zeolite exhibited a higher CO_2 adsorption capacity [15-17]. As reported by Dabbawala, due to the lower silica-to-aluminium ratio of Y zeolite, the higher total pore volume, and the interconnected micropore-mesoporous hierarchical structure, the CO_2 adsorption capacity of Y zeolite reaches 5.40 $mmol \cdot g^{-1}$ under the conditions of 298 K and 1 bar. However, the conventional industrial production of Y zeolite in the existing reports was synthesised using relatively expensive chemical raw materials. In addition, Y zeolite has excellent CO_2 adsorption performance at low temperatures, but not ideal at high temperatures [18]. In this paper, we use water quenching slag, a by-product of the iron and steel industry, to synthesise Y zeolite. The method has simple steps, low cost, a high synthesis yield, a short cycle and causes little pollution. The synthesised Y zeolite exhibited excellent adsorption performance for CO_2 at high temperatures (60-90 °C), which makes it possible for the adsorbent to be applied to capture CO_2 at the end of the steel plant.

In this study, water quenching slag was used as a raw material and Y zeolite was synthesised by the alkali fusion hydrothermal method. The effects of the crystallisation time, $n(SiO_2)/n(Al_2O_3)$ ratio, crystallisation temperature and $n(Na_2O)/n(Al_2O_3)$ ratio on the synthesis were investigated. The prepared NaY zeolite was characterised by different techniques, such as X-ray diffraction (XRD), Scanning electron microscopy (SEM) and scanning transmission electron microscopy (STEM). The adsorption performance of NaY zeolite for CO_2 and N_2 was measured, and its CO_2/N_2 selectivity was calculated. Finally, the thermodynamic analysis of NaY zeolite adsorption of CO_2 was carried out to explore its adsorption mechanism.

EXPERIMENTAL METHODS

Materials

The water quenching slag (WQS) was taken from the Bayuquan Branch of Anshan Iron and Steel Group Company. The chemical composition of WQS was shown in Table 1. Hydrochloric acid (36~38 %), ($NaAlO_2$), (NaOH), were purchased from Sinopharm Chemical Reagent. Ludox (SiO_2 > 30 %) was purchased from Guangzhou Suixin Chemical Co., Ltd.

Preparation of the precursor mixture

0.0984 g of $NaAlO_2$ and 1 g of NaOH was dissolved in 5.65 g of deionised water. Then 1.8 g of silica sol was slowly added to the solution of $NaAlO_2$ and NaOH, and after continuous stirring for 30 min, it was aged at room temperature for 6 h to obtain a precursor mixture. The molar ratio of substances in the mixture solution is $SiO_2:Al_2O_3:Na_2O:H_2O$ = 15:1:22:638.

Preparation of NaY zeolite

The NaY zeolite was synthesized by hydrothermal crystallization using acid-treated water quenching residue as the silicon source, NaOH and $NaAlO_2$ as solid bases. During the synthesis process, the molar ratio of substances in the crystallization liquid is controlled at $8SiO_2:Al_2O_3:8Na_2O:350H_2O$. As a typical step, the water quenching slag was fully ground to below 200 mesh. Place 10 g of water quenching slag and 120 ml of 4 $mol \cdot L^{-1}$ hydrochloric acid in a stirrer, heat and stir at 60°C for 2 hours to complete the acid leaching reaction. Then, the solid and supernatant liquid after the acid leaching reaction were separated. The solid after acid leaching was fully filtered and dried to obtain silicone gel powder. The chemical composition of silicone gel is shown in Table 1. Then, 0.765 g silicone gel powder and 0.5 g NaOH powder were mixed and calcined at 600 °C for 1 h. The cooled clinker, 10 ml deionized water and

Table 1. Chemical composition analysis of the silicon gel and water quenching slag (mass percentage).

	SiO_2	CaO	Al_2O_3	Fe_2O_3	Other
Silicone gel	97.80	0.56	0.58	0.10	0.96
Water quenching slag	31.00	41.90	14.99	1.97	10.14

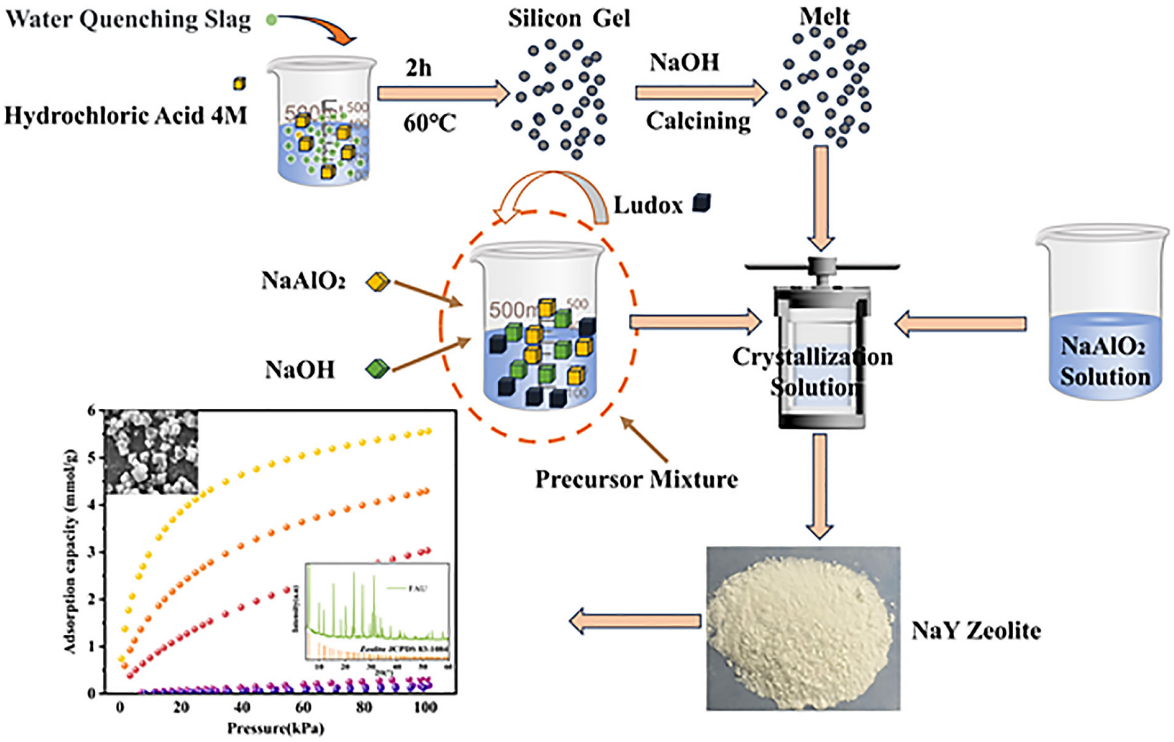

Figure 1. Chemical composition analysis of the silicon gel and water quenching slag (mass percentage).

0.3415 g $NaAlO_2$ were placed in beaker A, and stired at 60 °C for 30 minutes to obtain a slurry. Then add the previously synthesized precursor mixture to beaker A. The solution in beaker A was hydrothermally crystallized at 90 °C for 4 hours to obtain a white precipitate. After filtration, washing and drying, NaY zeolite was obtained. The synthesis process was shown in Figure 1.

Characterisation methods

The chemical composition of the water quenching slag and silicon gel was analysed by X-ray fluorescence (XRF) using a ZSX Primus II spectrometer (Rigaku, Japan). The crystalline properties of the samples were examined by X-ray diffraction (XRD) using a Shimadzu X-ray diffractometer. The relative XRD intensity representative of the crystallinity was determined according to ASTM D3906-91. The chemical bond information of the sample was measured by a Nicolet iS50 FTIR spectrometer (ThermoFisher, USA) in a wave number range of 4000 to 400 cm^{-1}. The microscopic morphology of the samples was examined by scanning electron microscope micrographs using a *JSM-IT800 microscope (Japanese Electron). The heat loss of the sample was checked by a STA449F3 synchronous thermal analyser at 10 ℃·min^{-1} from 35 ℃ to 800 ℃, and at N_2 (99.99 %) at 30 ml·min^{-1}. The measurement and characterisation of the adsorption isotherm of N_2 and CO_2 was conducted by a BSD-PS physical adsorption analyser (Beishide Instrument Technology (Beijing) Co., Ltd). The NaY zeolite was first vacuum degassed at 573 K for 2 h to release the adsorption sites of the sample. Then, the temperature was adjusted to the required adsorption temperature to obtain the CO_2 adsorption curve at the corresponding temperature. The adsorption isotherm of N_2 was obtained in the same way. The specific surface area of the zeolite was calculated by the Brunauer–Emmett–Teller (BET) method, and the pore volume was calculated by the Barret-Joyner-Hallender (BJH) method.

RESULTS AND DISCUSSION

Optimisation of the synthesis conditions

The zeolite was crystallized into two steps, included nucleation and crystal growth. The first is the nucleation stage, where the alkali fusion-treated silicone gel powder is mixed with $NaAlO_2$ solution and converted into soluble aluminosilicate. Silicon and aluminum dissolve in alkaline media (through hydrolysis), and the dissolved species condense into monomers, and then condense into polymers. The geopolymer at this time is an amorphous semi-crystalline aluminosilicate gel. Due to similar mechanisms, zeolite structures are often detected in geopolymer gels. Due to similarities in chemical composition, geopolymers are often considered precursors to zeolites, which can be synthesized by hydrothermal treatment. During the crystal growth process under hydrothermal conditions, this experiment systematically studied the effects of $n(SiO_2)/n(Al_2O_3)$ ratio, crystallization time, crystallization temperature and $n(Na_2O)/n(Al_2O_3)$ ratio on the synthesis of NaY zeolite.

Table 2. Synthesis conditions and crystallinity of the samples.

No	Crystallisation time (h)	$n(SiO_2)/n(Al_2O_3)$	Crystallisation temperature (℃)	$n(Na_2O)/n(Al_2O_3)$	NaY (crystallinity (%))
A1	4	8	90	8	–
A2	8	8	90	8	86.88
A3	12	8	90	8	87.68
A4	20	8	90	8	86.65
A5	24	1	90	8	87.15
B1	12	4	90	8	83.83
B2	12	8	90	8	91.74
B3	12	16	90	8	85.43
B4	12	20	90	8	–
B5	12	24	90	8	–
C1	12	8	70	8	87.15
C2	12	8	80	8	88.13
C3	12	8	90	8	91.74
C4	12	8	100	8	92.79
C5	12	8	110	8	88.3
D1	12	8	100	4	90.23
D2	12	8	100	6	91.97
D3	12	8	100	8	92.89
D4	12	8	100	10	86.95
D5	12	8	100	12	83.64

The effects of different conditions on the synthesis of NaY zeolite were are shown in Table 2.

Effect of the Crystallisation Time

The samples with the composition of $8SiO_2$:Al_2O_3: :$8Na_2O$:$350H_2O$ in the crystallisation solution was used to investigate the effect of crystallisation time on the synthesised zeolites at 100 °C. Figure 1 shows the XRD patterns of samples crystallised from 4 h to 24 h. It can be observed that the characteristic diffraction peaks of Y zeolite in the crystallisation solution are not obvious and the relative crystallinity is low from 4 h to 8 h. This is mainly due to the polymeric silicate units (D6R) that make up the Y zeolite which are more complex, larger, and sparser, and thus require longer crystallisation times [20]. Further extending the crystallisation time to 12 h, the characteristic peak intensity of NaY zeolite was the highest, indicating that the zeolite crystallisation was almost completed within 12 hours. As shown in Figure 2, the sample was very well-indexed with the standard zeolite (JCPDS: 83-1084). The diffraction peaks appearing at 6.2°, 10.1°,11.8°,15.5°, 20.1°, 23.3°, 26.5°, 30.9° and 33.6° are assigned to the (1 1 1), (2 2 0), (3 1 1), (3 3 1), (4 4 0), (5 3 3), (6 4 2), (751) and (6 6 4) lattice planes, respectively. However, when the crystallisation time was between 16 h to 24 h, the frameworks of Y zeolite began to dissolve, resulting in a decrease in the relative crystallinity.

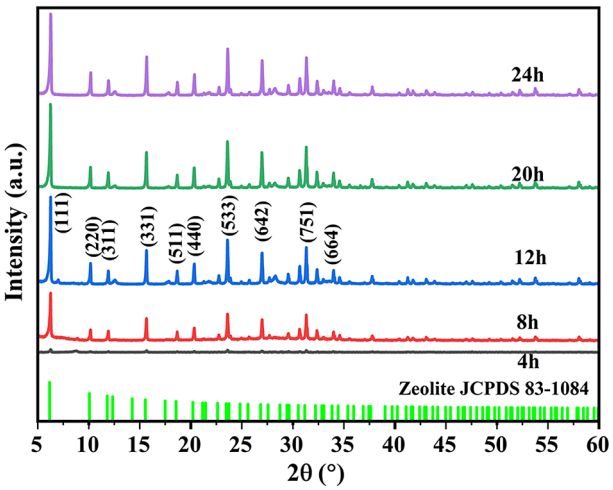

Figure 2. XRD patterns of the NaY zeolite synthesised at different crystallisation times.

Effect of $n(SiO_2)/n(Al_2O_3)$

In general, the ratio of silicon to aluminium in the raw material will be higher than that of the crystallised product, and the excess silicon will remain in the solution. The silicon-aluminium ratio of zeolite composition is characterised by the fact that a certain zeolite crystalline product can only be synthesised in a specific crystallisation area and within the range of silicon-alumina ratio. The mole oxide compositions of the gels were $xSiO_2$:Al_2O_3:$8Na_2O$:$350H_2O$, in which X varied from 4 to 24. The slurry was hydrothermally crystallised at 100 °C for 12 h. The effect of the $n(SiO_2)$:$n(Al_2O_3)$ in the crystallisation solution on the XRD patterns of the prepared zeolites are shown in Figure 3. In Figure 3, a single-phase zeolite NaY was formed at $n(SiO_2)$/ /$n(Al_2O_3)$ = 4. When this ratio increased to 8, the peak intensity of zeolite NaY was significantly strengthened, and the relative crystallinity of zeolite NaY also reached the maximum. A similar trend was reported by Nakhaei et al [23]. When the ratio exceeds 20, zeolite NaY was difficult to synthesise. The reason why high-silica Y zeolites are difficult to synthesise is that the crystal formation process is controlled by the reaction kinetics [26, 27]. The corresponding polysilicate and aluminate polycondensation reactions are difficult to crystallise due to high reaction activation energy and small reaction rate constant *k*.

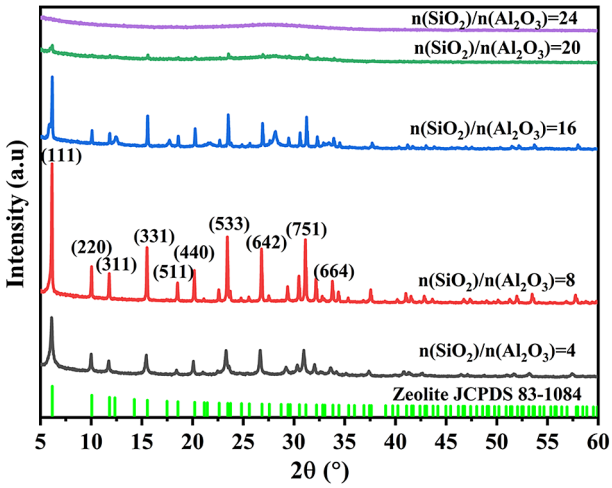

Figure 3. XRD patterns of NaY zeolite synthesised at different $n(SiO_2)/n(Al_2O_3)$.

Effect of the crystallisation temperature

The effect of the crystallisation temperature on the synthesised Y-zeolite crystallisation was investigated under the conditions of $8SiO_2$:Al_2O_3: $8Na_2O$:$350H_2O$, and a crystallisation time of 12 h. Figure 4 shows the XRD patterns of the zeolites at temperatures of 70 °C, 80 °C, 90 °C, 100 °C and 110 °C. The crystallisation temperature affects the nucleation process and the crystal growth process. The lower the temperature, the longer the crystallisation time will be. Y zeolite has been well synthesised at 70 °C to 90 °C. When the crystallisation temperature was increased to 100 °C, NaY zeolite with the highest purity and best crystallinity was obtained. When the temperature exceeds 100 °C, the crystallisation of Y zeolite showed a downward trend. It is worth noting that higher processing temperatures will produce larger

particle sizes for zeolites at a given crystallisation time [25]. Larger size zeolites are unfavourable for CO_2 adsorption, so we determined that the optimum crystallisation temperature of Y zeolite is 100 °C.

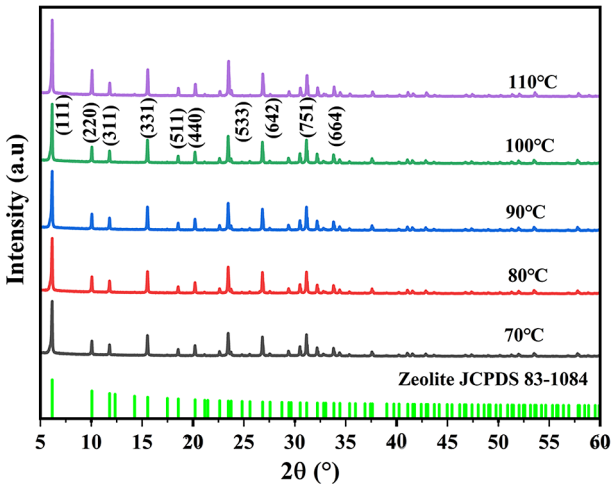

Figure 4. XRD patterns of NaY zeolite synthesised at different crystallisation temperatures.

Effect of $n(Na_2O)/n(Al_2O_3)$

Cations serve as structure-directing and charge-balancing roles in zeolite crystallisation. Under certain circumstances, Na^+ can guide the synthesis of Y zeolite. OH^- can promote the formation of the primary structure of zeolite and help form the bonds between the SiO_4 and AlO_4^- tetrahedra. The mole oxide compositions of the gels were $xNa_2O:Al_2O_3$: $8SiO_2:350H_2O$, in which X varied from 4 to 12. The slurry was hydrothermally crystallised at 100 °C for 12 h. The effect of the Na_2O ratio in the crystallisation solution on the XRD pattern of the prepared zeolites is shown in Figure 5. According to Figure 5, when $n(Na_2O)/n(Al_2O_3)$ was in the range of 4 to 12, the characteristic diffraction peaks of Y-type zeolite all exist. When enhancing the Na_2O content in the crystallisation solution, the relative crystallinity reaches its maximum at a ratio of 8. It is similar to what was reported by Nakhaei et al [23]. However, when $n(Na_2O)/n(Al_2O_3)$ was higher than 10, the intensity of NaY decreases significantly. It is well known that if the alkalinity in the crystallisation solution is too high, the zeolite framework will be partially dissolved, resulting in a decrease in crystallinity [24].

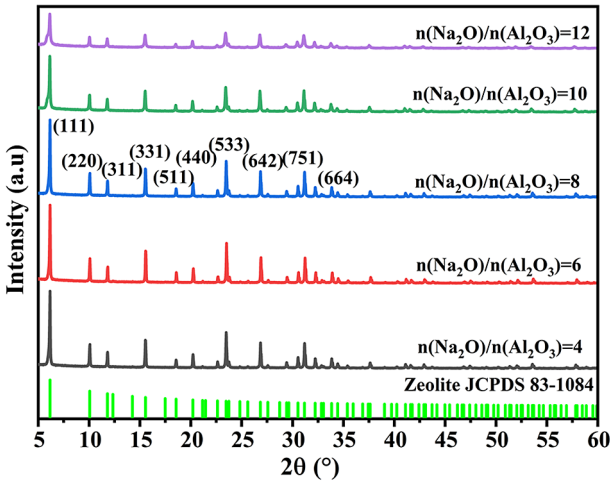

Figure 5. XRD patterns of NaY zeolite synthesised at different $n(NaO)/n(Al_2O_3)$.

As can be seen from Figure 6a, the water quenching slag particles are larger and unevenly distributed. After the acid treatment, the SiO_2 content in the silicone gel exceeds 97 %, and the microscopic morphology is also very different from that of water quenching slag, with a more regular shape (Figure 6b). The low-magnification and high-magnification SEM morphology of the Y-type zeolite is shown in the Figure 7. The synthesised Y-type zeolite has a uniform crystal grain size, which clearly exhibits the cubic crystal structure of the Y zeolite, has clear grain boundaries, and is evenly distributed without crystal grain aggregation. The image is consistent with that shown in the literature, indicating that the crystalli-

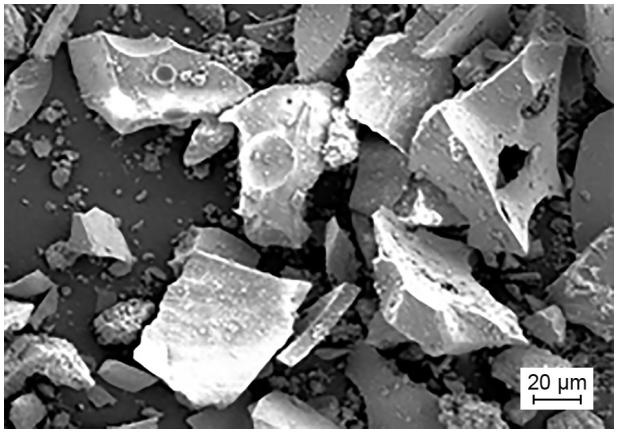

a)

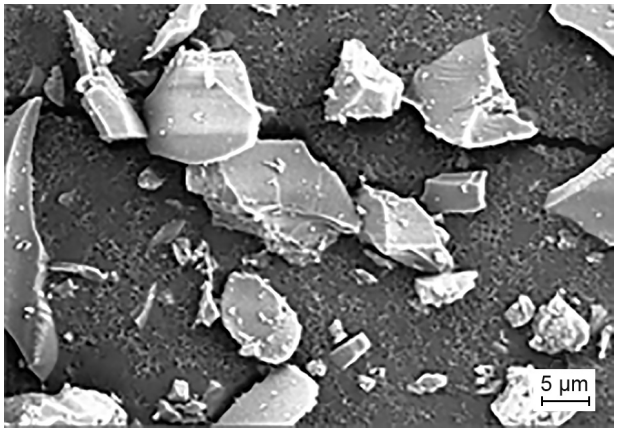

b)

Figure 6. SEM images of the water quenching slag (a) and silicon gel (b).

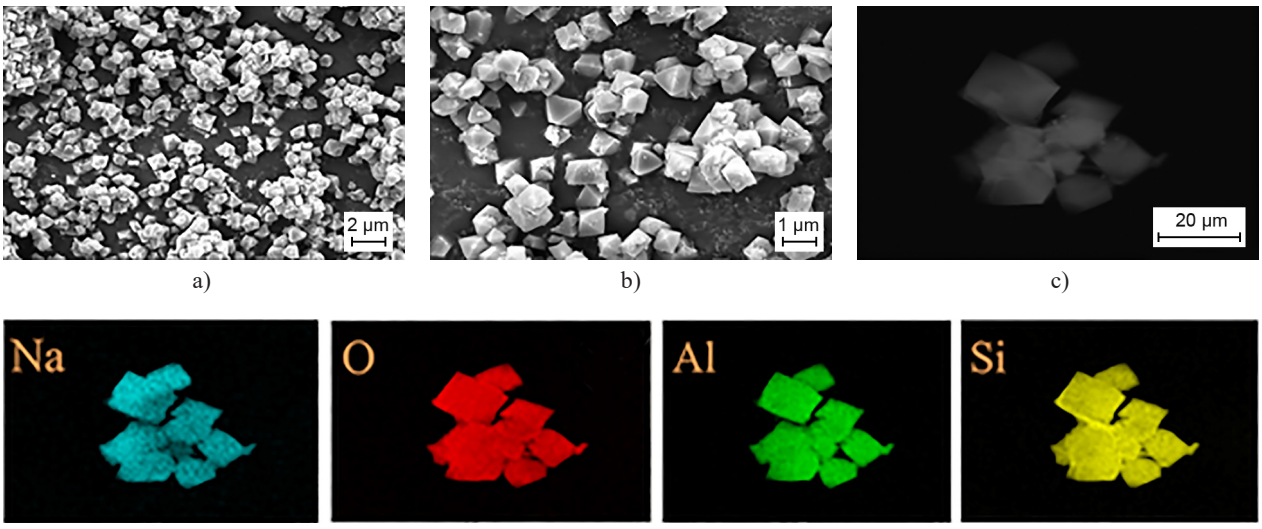

Figure 7. SEM images for NaY zeolite at low magnification (a) and high magnification (b), STEM-mapping image of NaY (c, d).

sation of Y zeolite under the experimental conditions is ideal [18, 19]. In addition, the elemental map image (Figure 7d and Figure 8a shows that the elements Na, Si, Al and O in the synthesised NaY zeolite not only exist, but are evenly distributed.

The Fourier-transform infrared spectroscopies of the synthesised Y-type zeolite is shown in Figure 8b. The peaks at around 3395 cm^{-1} and 1645 cm^{-1} are attributed to the H−O bond stretching vibration and bending vibration of absorbed water in zeolite, respectively. The characteristic peak at 441.98 cm^{-1} is produced by the bending vibration of Si−O and Al−O bonds. The characteristic peak at 566.37 cm^{-1} is produced by the stretching vibration of the tetrahedral structure. The characteristic peak at 681.65 cm^{-1} is produced by the symmetric stretching vibration of the silicon-oxygen tetrahedron. The characteristic peak at 964.98 cm^{-1} is caused by the anti-symmetry of the silicon-oxygen tetrahedron in the molecular sieve framework. The above shows that the synthesised samples definitely contain the structure of NaY zeolite [20].

The thermogravimetric analysis of the samples was performed to investigate the thermal stability of NaY zeolite. As can be seen in Figure 8c, d, the weight loss of NaY zeolite is between 30 % during the heating process. The TGA curve of the Y-type zeolite has an obvious weight loss peak before 300 °C, which is due to the abundant micropores in the NaY zeolite and the adsorption of water in the OH groups. After 300 °C, the weight of NaY zeolite did not change much, indicating that the prepared NaY zeolite had a relatively stable chemical structure [21].

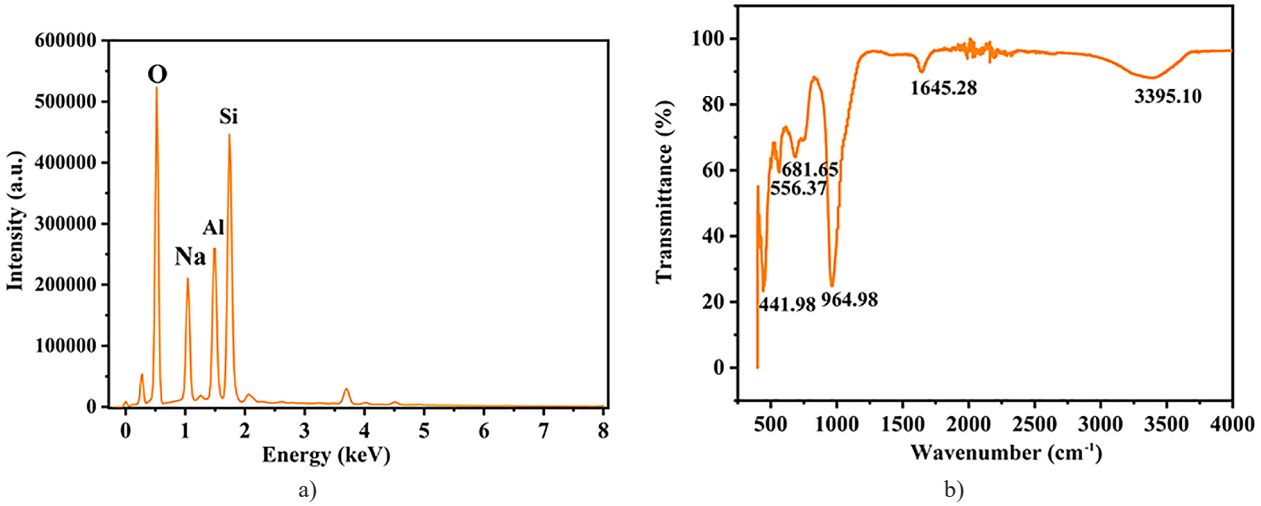

Figure 8. EDS analysis of NaY zeolite (a); FT-IR spectra of NaY zeolite (b); TGA curve of Y zeolite (c). *(Continue on next page)*

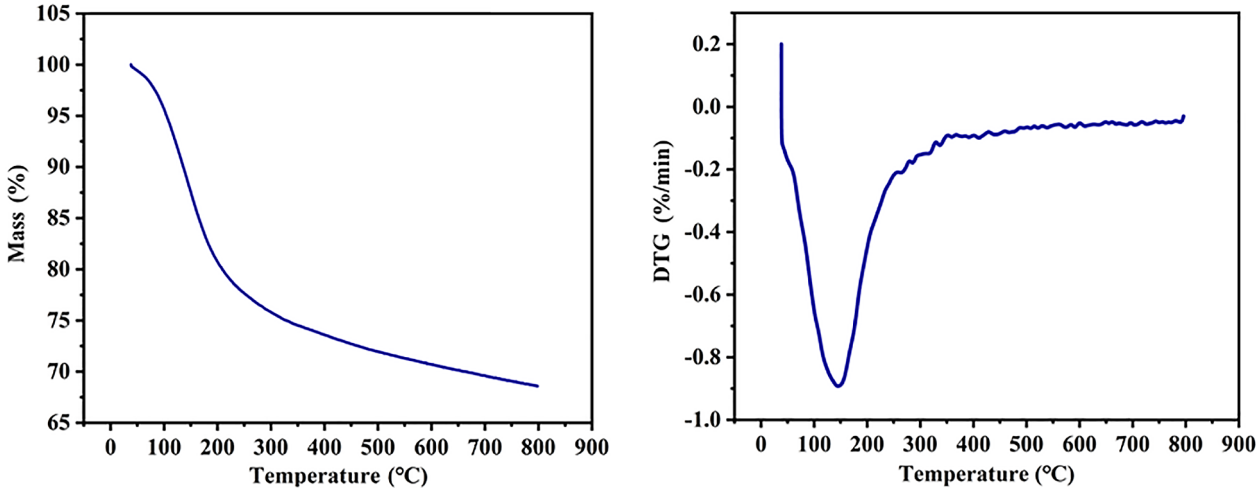

c) d)

Figure 8. TGA curve of Y zeolite (c); DTG curve of Y zeolite (d).

Gas adsorption performance research

The CO_2 and N_2 adsorption isotherms of NaY zeolite at 303, 333, and 363 K are shown in Figure 9. The adsorption capacity of CO_2 and N_2 tended to decrease with the increasing temperature and decreasing pressure. The sample exhibits typical physisorption behaviour, which was 5.56, 4.50, and 3.03 mmol·g^{-1} measured at 303 K, 333 K, and 363 K (100 kPa) using an BSD-PS analyser, respectively. Interestingly, in the low-pressure region (< 0.5 bar), the CO_2 adsorption capacity of NaY zeolite is close to 5 mmol·g^{-1}. Considering the working environment of NaY zeolite to be used in steel plants, it is suitable for separating CO_2 from the flue gas. The high CO_2 adsorption capacity of NaY zeolite is due to the interconnected hierarchical porous network, which reduces the resistance to CO_2 transport.[4] Similarly, NaY zeolite has the characteristics of a high specific surface area and total pore volume, which provide abundant CO_2 adsorption sites (Table 5). In addition, the Si/Al ratio of NaY zeolite is less than 4, which indicates the high Al content in the sample. Therefore, there is a higher number of acid-base sites in the sample. These acid-base sites will also increase the CO_2 adsorption capacity.

In order to determine the CO_2 adsorption selectivity of the sample, the N_2 adsorption was measured at 303 K, 333 K, and 363 K. Under atmospheric pressure, the N_2 adsorption capacity corresponding to the three temperatures is 0.32 mmol·g^{-1}, 0.17 mmol·g^{-1} and 0.12 mmol·g^{-1}, respectively, which is much lower than the CO_2 adsorption capacity under the same temperature conditions,

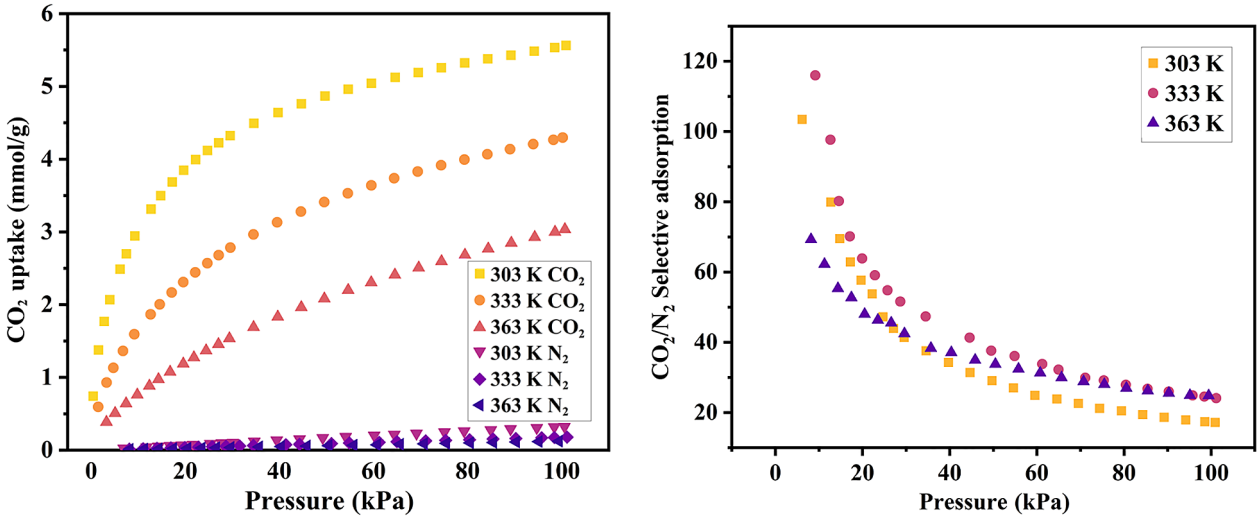

a) b)

Figure 9. Adsorption characteristics of NaY zeolite on CO_2 and N_2 at different temperatures and pressures (a), selectivity of CO_2/N_2 (b).

indicating that NaY zeolite has a good application prospect in CO_2/N_2 adsorption separation. According to the relevant literature, Equation 1 is used to calculate CO_2/N_2 selective adsorption.

$$s_p = \left(\frac{q_A}{q_B}\right) \tag{1}$$

where q_A is the quantity adsorbed per unit mass by gas A, q_B is the quantity adsorbed per unit mass by gas B at the selected pressure and temperature. Figure 9b shows the pure selectivity of CO_2/N_2, and it can be seen that the selectivity ratios of NaY zeolite at three temperatures are 17, 26 and 25 at atmospheric pressure, respectively. The CO_2/N_2 selectivity decreased with an increase in the temperature and total pressure. Due to the high adsorption and gas selectivity, the NaY zeolite synthesised in this experiment will be an excellent candidate adsorbent for the CO_2 capture in flue gas. The CO_2 adsorption capacity of NaY zeolite was also compared with the reported adsorbents studied for CO_2 adsorption (Table 3). Compared with K-CHA, Nano-zeolite, 2D-LTA, MOF-177, AEEA-ZSM-5, and NaA, NaY zeolite has a higher CO_2 adsorption capacity at more than 30 °C and 1 atmosphere.

Table 3. Comparison of the CO_2 adsorption capacities of NaY zeolite with the reported adsorbents.

Adsorbent	Temperature (°C)	1 bar Capacity ($mmol \cdot g^{-1}$)	Ref.
NaY	30	5.56	This work
	60	4.50	This work
	90	3.03	This work
K-CHA	30	2.42	[28]
	60	2.13	[28]
Nano-zeolite	20	4.81	[29]
2D-LTA	25	2.59	[30]
	100	1.12	[30]
MOF-177	55	4.6	[31]
AEEA-ZSM-5	48	4.44	[32]
NaA	30	3.68	[33]
	60	2.98	[33]

Fitting the adsorption thermodynamic model is an important method to analyse the adsorption type and adsorption mechanism. In this study, the Langmuir model, Freundlich model, and Toth model were used to fit the CO_2 adsorption curve of NaY zeolite. The Langmuir equation is shown in Equation 2.

$$q_e = \frac{q_m bp}{1 + bp} \tag{2}$$

where q_e is the adsorption capacity of the adsorption equilibrium, q_m is the saturated adsorption capacity of the adsorbent, b is the equilibrium constant and p is the equilibrium pressure of the adsorbate gas. The Freundlich equation is shown in Equation 3.

$$q_e = kp^{\frac{1}{n}} \tag{3}$$

where qe is the gas equilibrium adsorption capacity, p is the gas equilibrium state pressure, k is the adsorption intensity constant and n is affected by the adsorption temperature. The Toth equation is shown in Equation 4.

$$q_e = \frac{q_m bp}{[1 + (bp)^n]^{\frac{1}{n}}} \tag{4}$$

where q_e is the adsorption capacity reaching the adsorption equilibrium, q_m is the saturated adsorption capacity of the adsorbent, b is the equilibrium constant, p is the equilibrium pressure of the adsorbate gas and n constant is related to the unevenness of the surface of the adsorbent.

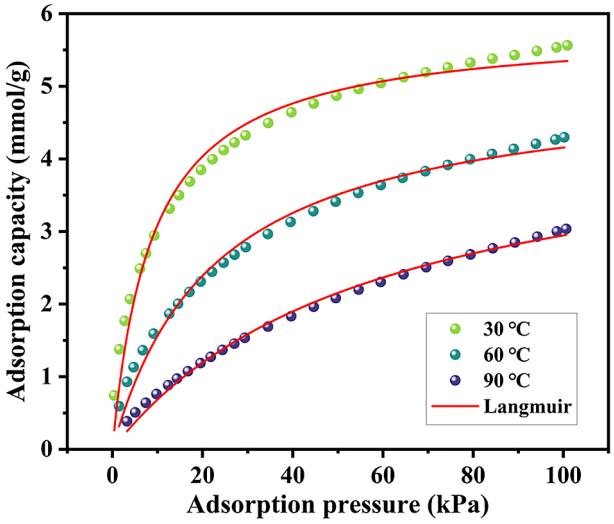

a)

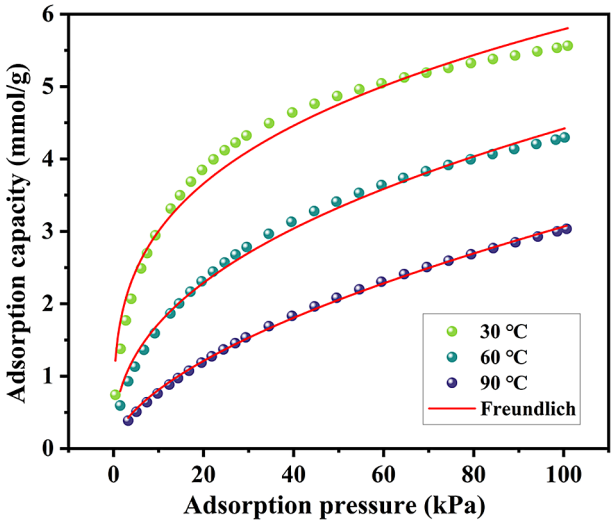

b)

Figure 10. Fitting adsorption thermodynamic models to adsorption curves at different temperatures: a) Langmuir model; b) Freundlich model. *(Continue on next page)*

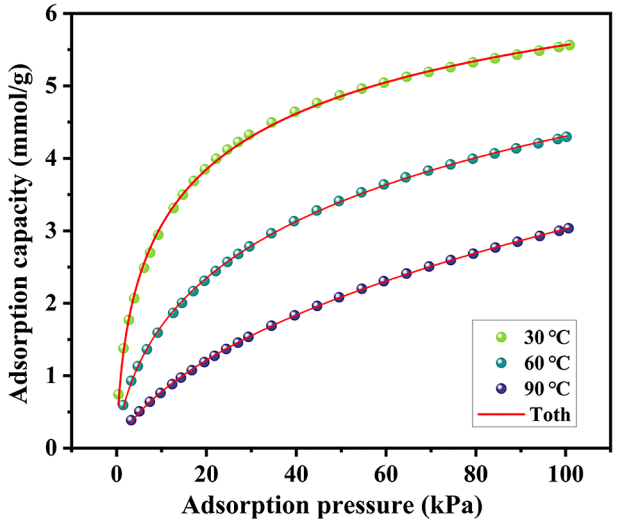

c)

Figure 10. Fitting adsorption thermodynamic models to adsorption curves at different temperatures: c) Toth model.

The thermodynamic fitting results of NaY zeolite are shown in Figure 10 and Table 4. From the perspective of correlation coefficient (R^2), the Toth model can better fit the experimental adsorption data. The Toth equation can well fit the change trend of the isothermal adsorption data of NaY zeolite to CO_2 at various temperatures. Since the Toth model is applicable to the situation where the adsorption surface of the adsorbent is non-uniform, it shows that the adsorption surface of the NaY zeolite is not uniform, and various pore sizes can adsorb CO_2. This phenomenon can also explain why NaY zeolite has a high CO_2 adsorption performance.

Table 4. Fitting parameters of different adsorption isotherm equations.

Isotherm model	Parameters	30 °C	60 °C	90 °C
Langmuir	q_m (mmol·g^{-1})	5.87	5.099	4.656
	b	0.113	0.044	0.017
	R^2	0.9782	0.9780	0.9941
Freundlich	k	1.557	0.673	0.215
	n	–0.285	–0.408	–0.577
	R^2	0.9762	0.9926	0.9986
Toth	q_m (mmol·g^{-1})	6.02	5.20	4.71
	b	0.418	0.092	0.008
	n	0.417	0.357	0.268
	R^2	0.999	0.999	0.999

Table 5. Surface and textural properties of NaY zeolite.

Sample	S_{BET} (m^2·g^{-1})	Total volume (m^3·g^{-1})	Micropore volume (m^3·g^{-1})	Ref.
NaY zeolite	838.88	0.35	0.31	This work
NaX zeolite	444	0.26	0.21	[34]
13X zeolite	405.2	0.294	0.169	[35]
Hierarchical zeolite-Y	773	0.39	0.26	[4]

Figure 11a shows the low-temperature BET adsorption-desorption curve of NaY zeolite. It can be seen from the curve that it belongs to typical type I adsorption. Mainly because the outer surface area of the sample is much smaller than the inner pore surface area of the zeolite. In the figure, the adsorption curve rises rapidly in the relatively low-pressure area. At this time, the pores in the adsorbent are quickly filled by the adsorbate. After being filled, there is a turning point, and the adsorption capacity becomes gentle, which is in line with the characteristics of the microporous structure of NaY zeolite. When the relative pressure is close to the saturation pressure, the adsorption amount will also increase rapidly. This is because there are certain gaps between the particles. When the pressure is close

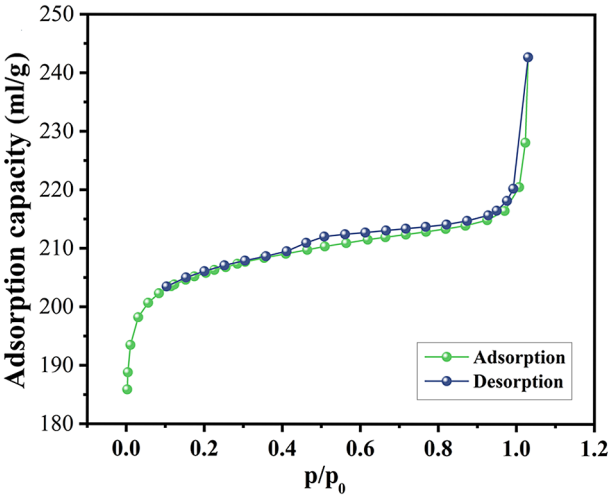

a)

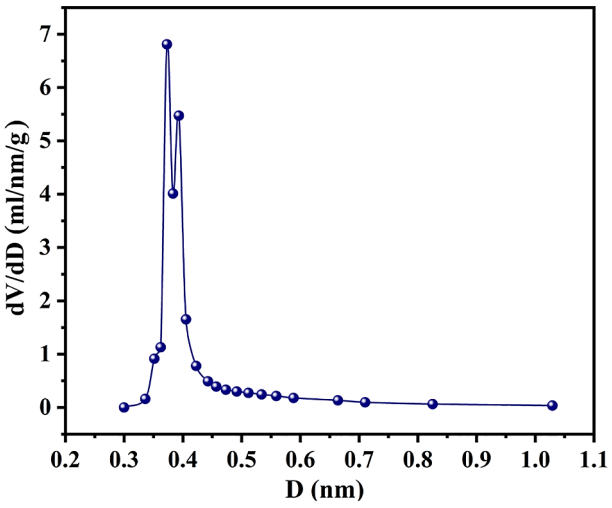

b)

Figure 11. N_2 adsorption/desorption isotherm at 77 K of zeolite-Y (a), size distribution of zeolite-Y (b).

to the saturation pressure, the particles will be tightly packed in the pore structure, thus appearing similar to the phenomenon of macropore adsorption, causing the isotherm to rise rapidly [22].

The pore size distribution of NaY zeolite drawn by the NLDFT method is shown in Figure 11b. The pore size is mainly distributed between 0.35 and 0.45 nm, and there are two peaks of the pore size, which also proves the rationality of the adsorption phase equilibrium of the Toth equation. In addition, the specific surface area of NaY zeolite is measured by T-Plot method, the micropore specific surface area of NaY zeolite is 809.1832 $m^2 \cdot g^{-1}$, and the external specific surface area is 29.6985 $m^2 \cdot g^{-1}$. Table 5 shows a comparison of the physical properties of NaY zeolite with other zeolites. The specific surface area and pore volume of NaY zeolite are much higher than other zeolites, supporting its potential as an efficient CO_2 capture adsorbent.

CONCLUSIONS

NaY zeolite was successfully prepared by the calcination and hydrothermal method using water quenching slag of industrial waste as the raw material. The effects of the crystallisation time, alkali concentration, crystallisation temperature and silicon-aluminium ratio of the reaction system on the synthesis of NaY zeolite molecular sieve were studied. Finally, the optimal synthesis conditions of the zeolite molecular sieve were obtained: the raw material element ratio in the reaction system is $n(SiO_2)/n(Al_2O_3) = 8$, $n(Na_2O)/n(Al_2O_3) = 8$, the crystallisation temperature is 100 °C, and the crystallisation time is 12 hours. The specific surface area of NaY zeolite prepared under these conditions is 838.88 $m^2 \cdot g^{-1}$, and the total pore volume is 0.3529 $mL \cdot g^{-1}$. At 303 K and 100 kPa, the CO_2 adsorption capacity of NaY zeolite reaches 5.56 $mmol \cdot g^{-1}$. Even at 333 K and 1 bar, the CO_2 adsorption capacity reaches 3 $mmol \cdot g^{-1}$, and the CO_2/N_2 selectivity exceeds 17, which is very beneficial for carbon capture in flue gas. In addition, this technical route also increases the added value of the slag, allowing steel plant slag to be recycled.

Acknowledgements

This work was funded by the "Seedling breeding" project of young scientific and technological talents in Liaoning Province (Grant No. LQ2020016).

REFERENCES

1. Guo H., Tang L., Yan B., Wan K., Li P. (2017): NaA zeolite derived from blast furnace slag: Its application for ammonium removal. *Water Science and Technology, 76(5)*, 1140-1149. doi: 10.2166/wst.2017.294
2. Ren Q., Zhang Y., Long Y., Zou Z., Pei J. (2018): Crystallisation behaviour of blast furnace slag modified by adding fly ash. *Ceramics International, 44(10)*, 11628-11634. doi: 10.1016/j.ceramint.2018.03.237
3. Majhi R. K., Nayak A. N. (2020): Production of sustainable concrete utilising high-volume blast furnace slag and recycled aggregate with lime activator. *Journal of Cleaner Production, 255,* 120188. doi: 10.1016/j.jclepro.2020.120188
4. Dabbawala A. A., Ismail I., Vaithilingam B. V., Polychronopoulou K., Singaravel G., Morin S., Berthod M., Al Wahedi Y. (2020): Synthesis of hierarchical porous Zeolite-Y for enhanced CO_2 capture. *Microporous and Mesoporous Materials, 303*, 110261. doi: 10.1016/j.micromeso.2020.110261
5. Lim J. Y., Kang Y. G., Sohn K. M., Kim P. J., Galgo S. J. C. (2022): Creating new value of blast furnace slag as soil amendment to mitigate methane emission and improve rice cropping environments. *Science of the Total Environment, 806*, 150961. doi: 10.1016/j.scitotenv.2021.150961
6. Li M., Zheng F., Wang J., Jia D., Mao X., Li P., Yuan Q., Zhen Q., Yu Y. (2023): Energy-saving production of high value-added foamed glass ceramic from blast furnace slag and hazardous wastes containing heavy metal ions. *Journal of Cleaner Production, 383,* 135544. doi: 10.1016/j.jclepro.2022.135544
7. Deng L., Jia R., Yun F., Zhang X., Li H., Zhang M., Jia X., Ren D., Li B. (2020): Influence of Cr_2O_3 on the viscosity and crystallization behavior of glass ceramics based on blast furnace slag. *Materials Chemistry and Physics, 240*, 122212. doi: 10.1016/j.matchemphys.2019.122212
8. Mancini A., Lothenbach B., Geng G., Grolimund D., Sanchez D., Fakra S. C., Dähn R., Wehrli B., Wieland E. (2021): Iron speciation in blast furnace slag cements. *Cement and Concrete Research, 140*, 106287. doi: 10.1016/j.cemconres.2020.106287
9. Miller S. A., John V. M., Pacca S. A., Horvath A. (2018): Carbon dioxide reduction potential in the global cement industry by 2050. *Cement and Concrete Research, 114*, 115-124. doi: 10.1016/j.cemconres.2017.08.026
10. Liu W., Aldahri T., Xu C., Li C., Rohani S. (2021): Synthesis of sole gismondine-type zeolite from blast furnace slag during CO2 mineralization process. *Journal of Environmental Chemical Engineering, 9(1)*, 104652. doi: 10.1016/j.jece.2020.104652
11. Hu Z.-P., Han J., Wei Y., Liu Z. (2022): Dynamic evolution of zeolite framework and metal-zeolite interface. *ACS Catalysis, 12(9)*, 5060-5076. doi: 10.1021/acscatal.2c01233
12. Deng C., Zhang J., Dong L., Huang M., Li B., Jin G., Gao J., Zhang F., Fan M., Zhang L. (2016): The effect of positioning cations on acidity and stability of the framework structure of Y zeolite. *Scientific Reports, 6(1)*, 23382. doi: 10.1038/srep23382
13. Zhou W., Zhou A., Zhang Y., Zhang C., Chen Z., Liu L., Zhou Y., Wei Q., Tao X. (2019): Hydrodesulfurization of 4,6-dimethyldibenzothiophene over NiMo supported on Ga-modified Y zeolites catalysts. *Journal of Catalysis, 374*, 345-359. doi: 10.1016/j.jcat.2019.05.013
14. Kumar S., Bera R., Das N., Koh J. (2020): Chitosan-based zeolite-Y and ZSM-5 porous biocomposites for H_2 and CO_2 storage. *Carbohydrate Polymers, 232*, 115808. doi: 10.1016/j.carbpol.2019.115808

15. Jedli H., Almoneef M., Mbarek M., Jbara A., Slimi K. (2022): Adsorption of CO_2 onto zeolite ZSM-5: Kinetic, equilibrium and thermodynamic studies. *Fuel, 321*, 124097. doi: 10.1016/j.fuel.2022.124097
16. Okello F. O., Fidelis T. T., Agumba J., Manda T., Ochilo L., Mahmood A., Pembere A. (2023): Towards estimation and mechanism of CO_2 adsorption on zeolite adsorbents using molecular simulations and machine learning. *Materials Today Communications, 36*, 106594. doi: 10.1016/j.mtcomm.2023.106594
17. Kwon D.-i., Kim J.-C., Lee H., Lee W., Jo C. (2022): Engineering micropore walls of beta zeolites by post-functionalization for CO_2 adsorption performance screening under humid conditions. *Chemical Engineering Journal, 427*, 131461. doi: 10.1016/j.cej.2021.131461
18. Walton K. S., Abney M. B., LeVan M. D. (2006): CO_2 adsorption in Y and X zeolites modified by alkali metal cation exchange. *Microporous and Mesoporous Materials, 91(1-3)*, 78-84. doi: 10.1016/j.micromeso.2005.11.023
19. Yin T., Meng X., Jin L., Yang C., Liu N., Shi L. (2020): Prepared hydrophobic Y zeolite for adsorbing toluene in humid environment. *Microporous and Mesoporous Materials, 305*, 110327. doi: 10.1016/j.micromeso.2020.110327
20. Bu N., Liu X., Song S., Liu J., Yang Q., Li R., Zheng F., Yan L., Zhen Q., Zhang J. (2020): Synthesis of NaY zeolite from coal gangue and its characterization for lead removal from aqueous solution. *Advanced Powder Technology, 31(7)*, 2699-2710. doi: 10.1016/j.apt.2020.04.035
21. Wei F., Guo X., Bao W., Chang L., Liao J. (2022): Metal Modified NaY Zeolite as Sorbent for the Ultra-Deep Removal of Thiophene in Simulated Coke Oven Gas. *Energies, 15(7)*, 2620. doi: 10.3390/en15072620
22. Awala H., Gilson J.-P., Retoux R., Boullay P., Goupil J.-M., Valtchev V., Mintova S. (2015): Template-free nanosized faujasite-type zeolites. *Nature Materials, 14(4)*, 447-451. doi:10.1038/nmat4173
23. Nakhaei Pour A., Mohammadi A. (2021): Effects of synthesis parameters on organic template-free preparation of zeolite Y. *Journal of Inorganic and Organometallic Polymers and Materials, 31(6)*, 2501-2510. doi: 10.1007/s10904-021-01926-1
24. Tran-Nguyen P. L., Ly K.-P., Thanh L. H. V., Angkawijaya A. E., Santoso S. P., Tsai M.-L., Ju Y.-H. (2021): Facile synthesis of zeolite NaX using rice husk ash without pretreatment. *Journal of the Taiwan Institute of Chemical Engineers, 123*, 338-345. doi: 10.1016/j.jtice.2021.05.009
25. Purnomo C. W., Salim C., Hinode H. (2012): Synthesis of pure Na–X and Na–A zeolite from bagasse fly ash. *Microporous and Mesoporous Materials, 162*, 6-13. doi: 10.1016/j.micromeso.2012.06.007
26. Kacirek H., Lechert H. (1975): Growth of the zeolite type NaY. *The Journal of Physical Chemistry, 79(15)*, 1589-1593. doi: 10.1021/j100582a024
27. Kacirek H., Lechert H. (1976): Rates of crystallization and a model for the growth of sodium-Y zeolites. *The Journal of Physical Chemistry, 80(12)*, 1291-1296.doi:10.1021/j100553a006
28. Gong H., Liu W., Liu L., Goyal N., Xiao P., Li G., Wei Y., Du T. (2019): In-situ synthesis of an excellent CO_2 capture material chabazite. *Journal of the Taiwan Institute of Chemical Engineers, 103*,160-166. doi: 10.1016/j.jtice.2019.07.006
29. Pham T.-H., Lee B.-K., Kim J., Lee C.-H. (2016): Enhancement of CO_2 capture by using synthesized nano-zeolite. *Journal of the Taiwan Institute of Chemical Engineers, 64*, 220-226. doi: 10.1016/j.jtice.2016.04.026
30. Shen J., Sun Q., Cao J., Wang P., Jia W., Wang S., Zhao P., Wang Z. (2022): A lamellar structure zeolite LTA for CO_2 capture. *New Journal of Chemistry, 46(14)*, 6720-6728. doi: 10.1039/D1NJ05908D
31. Gaikwad S., Kim Y., Gaikwad R., Han S. (2021): Enhanced CO_2 capture capacity of amine-functionalized MOF-177 metal organic framework. *Journal of Environmental Chemical Engineering, 9(4)*, 105523. doi: 10.1016/j.jece.2021.105523
32. Cheng H., Song H., Toan S., Wang B., Gasem K. A., Fan M., Cheng F. (2021): Experimental investigation of CO_2 adsorption and desorption on multi-type amines loaded HZSM-5 zeolites. *Chemical Engineering Journal, 406*,126882. doi: 10.1016/j.cej.2020.126882
33. Zhou X., Shi S., Ding B., Jia H., Chen P., Du T., Wang Y. (2023): Optimization of preparation of NaA zeolite from fly ash for CO_2 capture. *Environmental Science and Pollution Research, 30(46)*, 102803-102817. doi: 10.1007/s11356-023-29648-6
34. Lu X., Liu L., Liu H., Tian G., Peng G., Zhuo L., Wang Z. (2022): Zeolite-X synthesized from halloysite nanotubes and its application in CO_2 capture. *Journal of the Taiwan Institute of Chemical Engineers,133*, 104281. doi: 10.1016/j.jtice.2022.104281
35. Kongnoo A., Tontisirin S., Worathanakul P., Phalakornkule C. (2017): Surface characteristics and CO_2 adsorption capacities of acid-activated zeolite 13X prepared from palm oil mill fly ash. *Fuel, 193*, 385-394. doi: 10.1016/j.fuel.2016.12.087